

Materials Research Express



PAPER

Modeling of thin film explosive boiling—surface evaporation and electron thermal conductivity effect

V I Mazhukin¹, A A Samokhin², A V Shapranov¹ and M M Demin¹

¹ Keldysh Institute of Applied Mathematics, RAS, Moscow, Russia

² A. M. Prokhorov General Physics Institute, RAS, Moscow, Russia

E-mail: vim@modhef.ru

Keywords: evaporation, explosive boiling, spinodal decomposition, critical point, molecular dynamics, laser

Abstract

Phase transition in a thin liquid Al film during its rapid (sub) nanosecond homogeneous heating is studied in the framework of molecular dynamics simulation with electron thermal conductivity. The results are compared with our previous results without consideration of electron thermal conductivity. Surface evaporation leads to surface cooling and this effect is more pronounced at lower heating rates in the case without electron thermal conductivity. For the case with electron thermal conductivity, the obtained results suggest the existence of four different regimes of film behavior depending on the heating rate: quasi-stationary surface evaporation regime with relatively small fluctuations at the low heating rates, explosive (volume) boiling which is initiated as growth of a single fluctuation, spinodal decomposition with many fluctuations growing simultaneously and supercritical fluid expansion with no pronounced fluctuations at the high heating rates. Our calculations also show that the duration and magnitude of the explosive boiling pressure pulse, which occurs at the threshold heating rate, are about 0.3 ns and one third of the critical pressure value, respectively. Information of this kind is needed to determine the optimal conditions for the measurement of the critical parameters of different materials in laser ablation experiments.

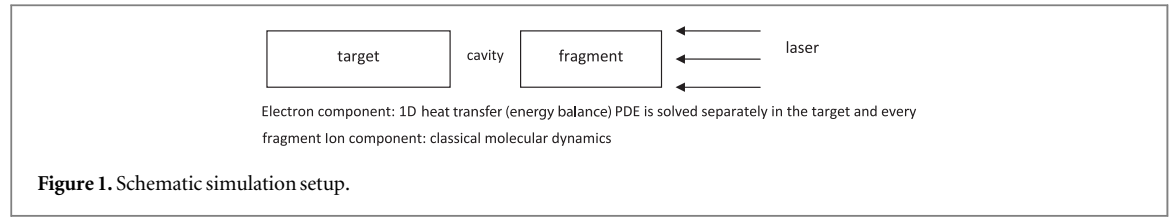
1. Introduction

Laser ablation has been investigated for many decades because of its practical importance as well as some unresolved fundamental questions in the non-equilibrium behavior of rapidly heated condensed matter (see, e.g. [1–16], and references therein). Among these questions there are the problems of metal-dielectric transition in the subcritical region and possible manifestation of the critical parameters in laser ablation experiments.

Now it is clear that the well-defined spinodal line as it appears in the Van-der-Waals equation of state (EoS) can barely be observed during the non-equilibrium liquid–vapor phase transition because of the rapid growth of fluctuations in the superheated metastable state. The EoS contains no time parameter while the experimental superheating limit which can be considered in some sense as a spinodal-like analog is clearly time dependent. In such conditions, the determination of the critical parameters in laser ablation experiments is not expected to be a very simple problem. Otherwise it could have been solved many years ago.

In [2] it was suggested that investigation of explosive boiling can be helpful in determination of the critical pressure because this process can occur only at an undercritical pressure in the phase transition region. Explosive boiling is mentioned in many papers (see references in [3–9]) but, to our knowledge, there is no sufficient information about the pressure behavior during this process.

In the present paper we investigate the phase transitions in a rapidly heated thin liquid Al film in the framework of molecular dynamics simulation with electron thermal conductivity [13]. This study continues our recent investigations [14] where some details of the thin film behavior during and after its rapid homogeneous heating with the rate of 2–100 K ps^{−1} are presented for the case without electron thermal conductivity.



2. Model and computational method

The process of laser action on metal targets (films) has a number of features associated with the presence of gas of free collectivized electrons. Therefore, metal targets are usually considered as two interacting components—electronic and atomic/ionic. Electronic component plays an important role, because it determines the high thermal conductivity value of the metal and it is where laser energy is directly deposited. Then the energy is transferred to the atomic component via electron-atomic collisions. The scheme of the laser action on a metal film with homogeneous phase transformations of the substance is shown in figure 1. Mathematical description of laser action in this paper, by analogy with [7, 13], is performed within the framework of combined atomistic-continuum model, in which the continuum energy equation is used for the electronic component, and the behavior of atomic components is described within the framework of classical molecular dynamics.

We consider behavior of a thin liquid Al film which is initially equilibrated with its saturated vapor at the temperature of $T = 6400$ K. This starting value of temperature was chosen to minimize the time of calculations. The initial film thickness through the x axis is $L = 48$ nm with the particle and mass density $n = 2.85 \cdot 10^{22} \text{ cm}^{-3}$ and $\rho = 1.28 \text{ g cm}^{-3}$ respectively. The overall number of particles is 96 000 and the length of calculation area is 268 nm in that direction. The periodic boundary conditions are used in the film plane with the dimensions of 8×8 nm. At the moment of time $t = 0$, free vapor expansion begins simultaneously with heating of the film at the effective energy deposition rate of $q = 2 \div 100 \text{ K ps}^{-1}$. At such energy deposition rates, the electron and ion temperatures differ but only slightly.

In the considered case of a thermally thin and optically thick film with the initial absorption length of 12.5 nm, this heating rate can be approximately written as $q = I\delta/3k_B nL$, where I is the incident laser intensity, k_B is the Boltzmann constant and $\delta = 0.98$ denotes the absorbed part of the laser intensity (because about 2% of the laser energy goes out from the back side of the film). For $q = 5 \text{ K ps}^{-1}$, this yields $I = 29 \text{ MW cm}^{-2}$.

The calculation procedure is essentially the same as in [7] with the interatomic potential given in [10]. The interatomic potential is chosen in the form of EAM potential written as

$$U(\vec{r}_1 \dots \vec{r}_N) = \frac{1}{2} \sum_{\substack{i,j=1 \\ i \neq j}}^N \phi(r_{ij}) + \sum_{i=1}^N f(\rho_i),$$

where $\phi(r_{ij})$ is the pair part of the potential, $f(\rho_i)$ is the embedding part, ρ_i is the total electron density of i th atom:

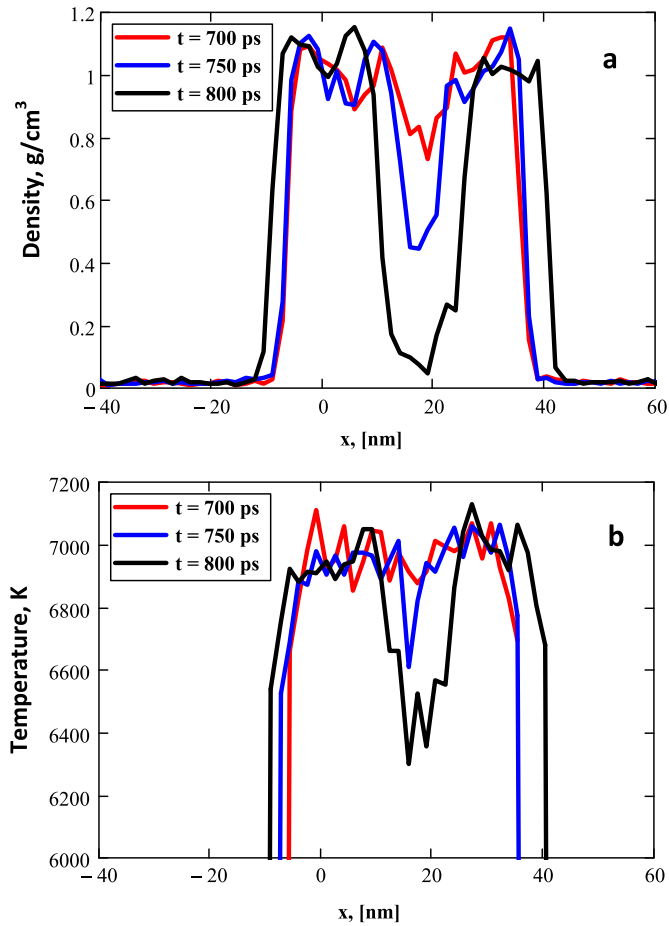
$$\rho_i = \sum_{\substack{j=1 \\ j \neq i}}^N n(r_{ij})$$

The authors of [10] used the following dependences as the pair and embedding parts of the potential and for the electron density:

$$\phi(r) = \begin{cases} 0, & r \geq r_c \\ \left(\frac{1}{a_1 r^2} - a_2 \right) (a_1 r^2 - a_1 r_c^2)^{10} \\ \quad \times \left[(a_1 r^2 - a_1 r_c^2)^6 + a_3 (a_1 r^2)^6 \right], & r < r_c \end{cases}$$

Table 1. Parameterization of EAM potential.

a_1	2.927 522 817 659 803 6	b_1	8.110 600 093 163 700 6	c_1	0.580 029 424 324 108 64
a_2	5.102 801 480 416 215 6	b_2	−334.574 937 446 235 03	c_2	8.298 118 542 206 363 9
a_3	111.377 422 368 935 90	b_3	14.868 297 626 731 845		
		b_4	1.608 095 393 177 309 0		

**Figure 2.** Film density (a) and temperature (b) distributions at 5 K ps^{−1} heating rate.

$$f(\rho) = \frac{b_1 \rho \cdot [b_2 + (b_3 + \rho)^2]}{1 + b_4 \rho},$$

$$n(r) = \begin{cases} 0, & r \geq r_c \\ \frac{c_1 \cdot (r^2 - r_c^2)^2}{1 + (c_2 r^2)^3}, & r < r_c \end{cases}$$

Here $r_c = 0.6875$ nm is the cutoff radius of the potential. The parameterization of these functions is listed in table 1.

Additional calculation details are presented in [13, 14]. For the considered interatomic potential, the critical temperature is $T_c = 7600$ K, the critical pressure is $P_c = 0.14$ GPa, and the critical density is $\rho_c = 0.5$ g cm^{−3}.

We conducted a series of test calculations to determine the optimum parameters providing convergence of the results. In the end, we determined the timestep (1 fs) and the target cross-section (5 nm × 5 nm).

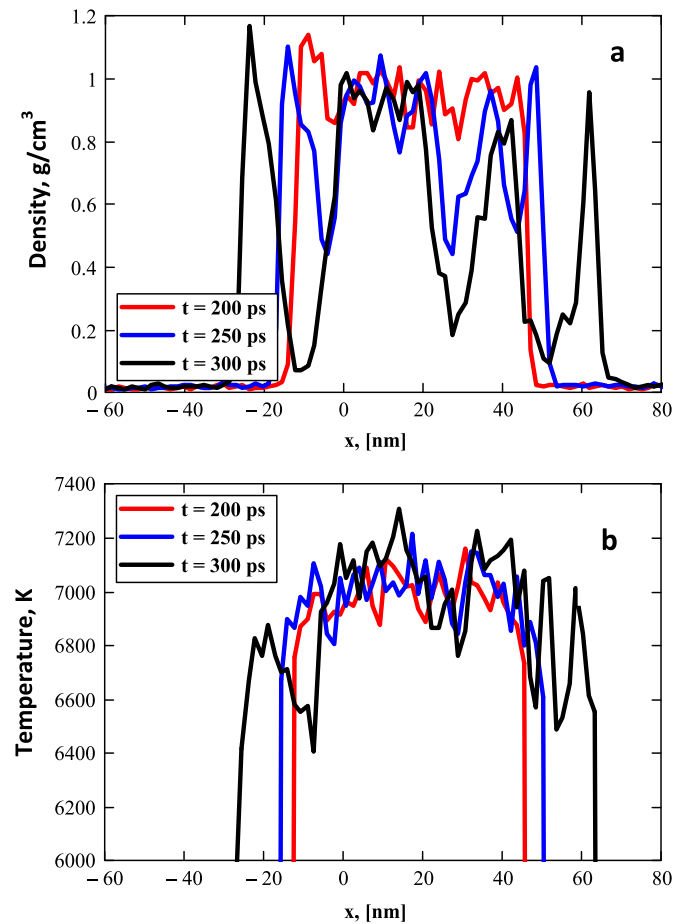


Figure 3. Film density (a) and temperature (b) distributions at 8.8 K ps^{-1} heating rate.

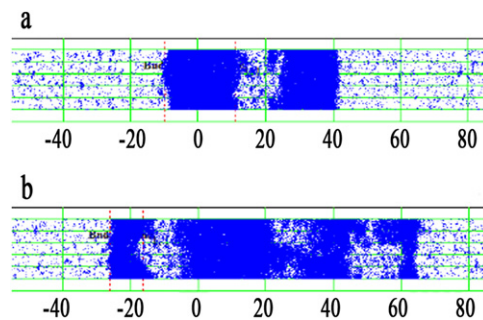


Figure 4. Snapshots of the expanding film at 5 K ps^{-1} heating rate, 800 ps (a) and 8.8 K ps^{-1} , 300 ps (b).

3. Results and discussion

Figure 2 shows the atomic density and temperature distributions at $t = 700, 750$ and 800 ps in the film with the effective heating rate of 5 K ps^{-1} . It is evident that the real temperature rise is strongly diminished due to cooling by surface evaporation and the film nearly reaches the steady state regime with relatively small temperature variations before the volume phase transition begins. The temperature drop clearly visible in the middle of the film at the very beginning of the phase transition (figure 2(b)) corresponds to negative heat capacity value which arises after the crossing with the spinodal in the continuous EoS.

It is worth noting that the outer film sides retain their approximate planarity in the considered space-time scale because the evaporation front instabilities [17] have no time to develop. On the other hand, the new boundaries inside the film are rougher due to the growth of density fluctuations just before the explosive boiling begins.

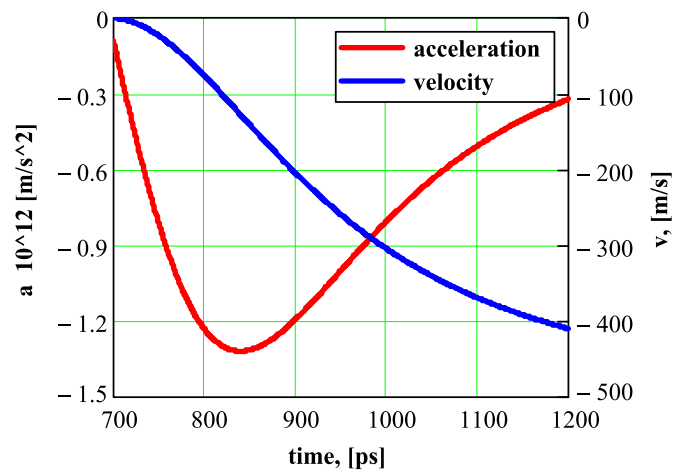


Figure 5. Velocity and acceleration of the left film fragment from figure 2(a).

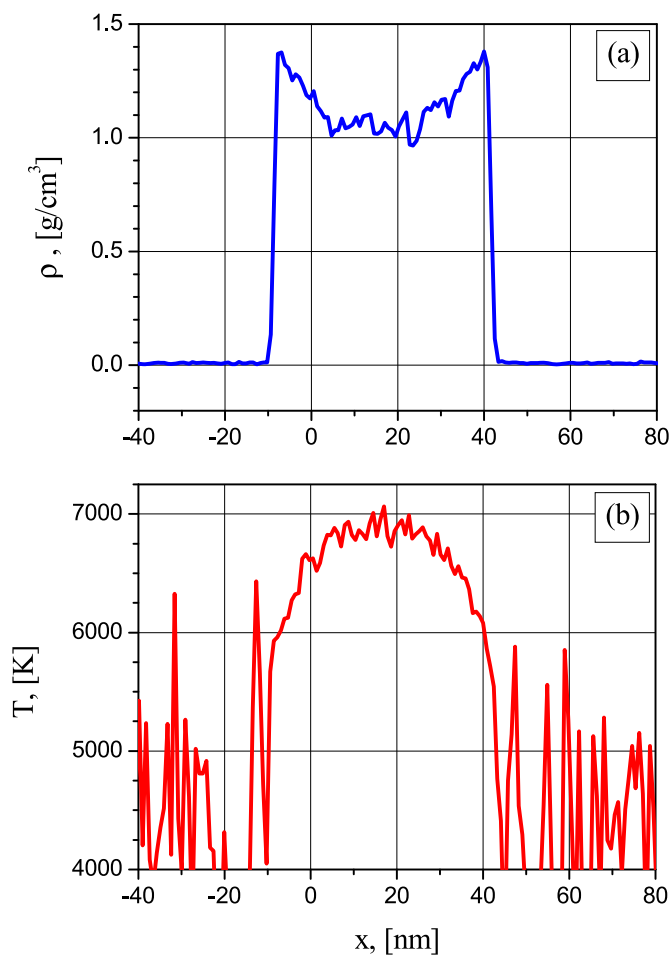


Figure 6. Film density (a) and temperature (b) distributions at 4 K ps^{-1} heating rate (dielectric case, 240 ps).

In the considered case the film disintegrates into two fragments, whose movements are determined by the surface pressure difference at their inner and outer sides. The positive pressure jump inside the film is determined by the explosive boiling process—in contrast to the spallation cases [7, 16] where the fragmentation is induced by the negative pressure value arising after absorption of shorter laser pulses. It should be also be mentioned that the explosive boiling process considered here with the time-dependent pressure and temperature behavior differs from the rapid volume growth in NPT simulations [6] because of different conditions in their realizations.

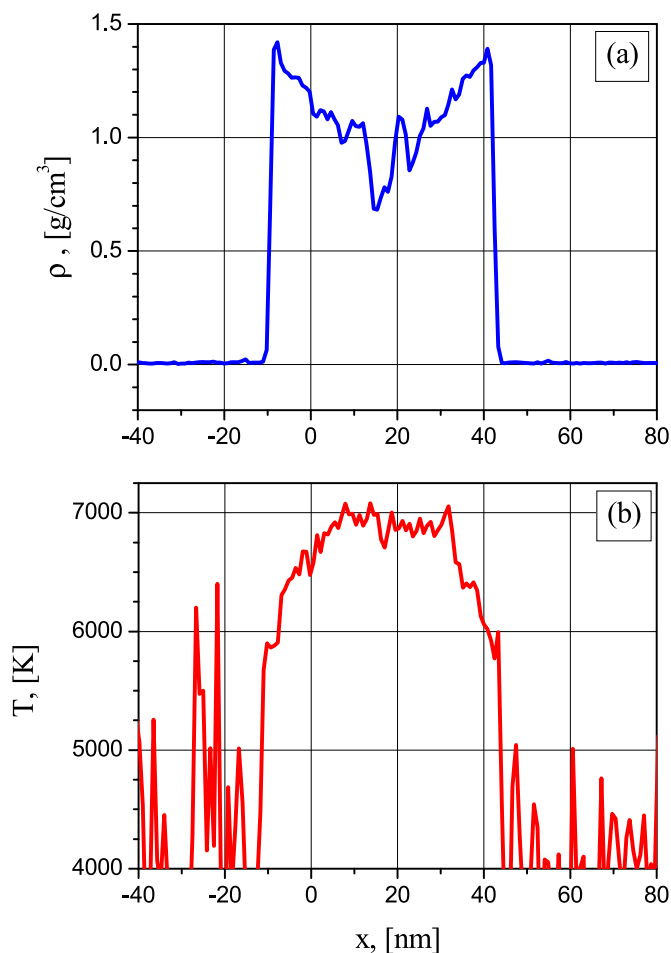


Figure 7. Film density (a) and temperature (b) distributions at 4 K ps^{-1} heating rate (dielectric case, 280 ps).

At the higher effective heating rate (figure 3) the phase transition in the superheated liquid gives rise to the formation of several fragments with less defined boundaries (except for the outer surfaces due to surface evaporation effect). The snapshots in figure 4 demonstrate the difference in the film evolution at 5 K ps^{-1} and 8.8 K ps^{-1} heating rates. This morphological change in the density distributions can be interpreted as a transition from the explosive boiling picture to spinodal decomposition which occurs at the larger superheating.

From the movement of these two fragments one can obtain the evolution of the explosive boiling pressure which is approximately proportional to the acceleration of a fragment. The time dependence of the velocity and acceleration of the left fragment are given in figure 5, which shows that the pressure pulse duration is 300 ps with the maximum near 850 ps. The beginning of the fast velocity growth is clearly visible also in figures 2 and 3 where the thickness of the films rapidly increases after 750 ps and 250 ps, respectively.

MD calculations provide the maximum pressure value of 0.055 GPa in the vapor cavity and 0.02 GPa at the outer fragment surface. These pressure values are approximately the same as in the case of the heating rate of 8.8 K ps^{-1} .

Similar parameters for the pressure pulse were also obtained in [14] at the heating rate of 4 K ps^{-1} for the film without electron thermal conductivity. Such a dielectric state can be realized if the metal–dielectric transition (see [1, 18] and references therein) occurs in the vicinity of the critical point where the film density is considerably lower than at room or melting temperatures.

In the dielectric film with no electron thermal conductivity and the same interatomic interaction, the surface evaporation effect is more pronounced giving rise to concave density distribution and convex temperature distribution across the film [14], as is shown in figures 6 and 7 for the heating rate of 4 K ps^{-1} at the moments 240 and 280 ps, respectively. Due to this effect, the density distribution in the expanding film retains clearly visible border peaks even at 40 K ps^{-1} heating rate when the main part of the distribution becomes convex as it should be in the case of the supercritical fluid expansion. At 100 K ps^{-1} , such peaks are barely visible and the film behavior is completely determined by the supercritical fluid expansion with no pronounced fluctuations.

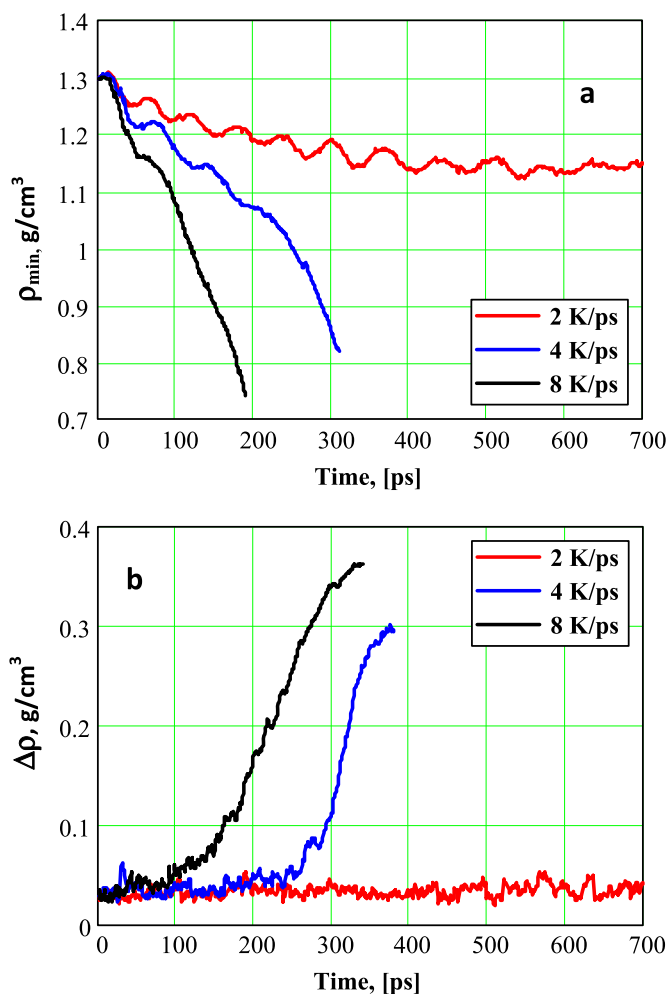


Figure 8. Minimal film density (a) and its fluctuations (b) at different heating rates.

Evolutions of the density minimum and temperature maximum obtained with the help of parabolic distribution interpolation are shown in figures 8, 9 for 2, 4 and 8 K ps^{-1} heating rates together with the fluctuations determined as the root-mean-square deviation from the interpolated minimum and maximum values. At 2 K ps^{-1} , the film density and temperature demonstrate (quasi)steady-state evolution with practically constant fluctuation level. The density and temperature oscillations visible in figures 8, 9 are probably due to acoustic vibrations in the film (see, e.g. [11, 15]).

At higher heat deposition rates, surface evaporation cooling is not sufficient to prevent the temperature rise which results in explosive boiling. The beginning of this process is marked with fast fluctuation growth (figures 8(b), 9(b)) which can be used to determine the superheating limit. From figures 8, 9 one obtains at this limit the values of density 0.82 g cm^{-3} and 0.74 g cm^{-3} and temperature 7000 K and 7160 K at 4 and 8 K ps^{-1} respectively.

The fast fluctuation growth near the superheating limit can also be obtained using constant pressure molecular-dynamics simulations [6]. However, such a procedure gives no information about the pressure behavior in the explosive boiling process under consideration.

In the recent paper ‘Time-resolved dynamics of nanosecond laser-induced phase explosion’ [9] the explosion (explosive boiling) is associated with the observation of the nearly doubled shock wave pressure value in the surrounding air above the irradiated Al target. For unambiguous interpretation of such experiments, however, it is necessary also to consider plasma formation effects in laser ablation process [18, 19].

Modeling [20, 21] of action of a laser pulse with nanosecond duration made it possible to reveal complex dynamics of the processes and spatial-time structure of laser-plasma plume in the evaporated material. Interaction of the plasma plume with the target surface results in a significant increase in pressure (by 2–10 times as compared to the recoil pressure) on the evaporating surface.

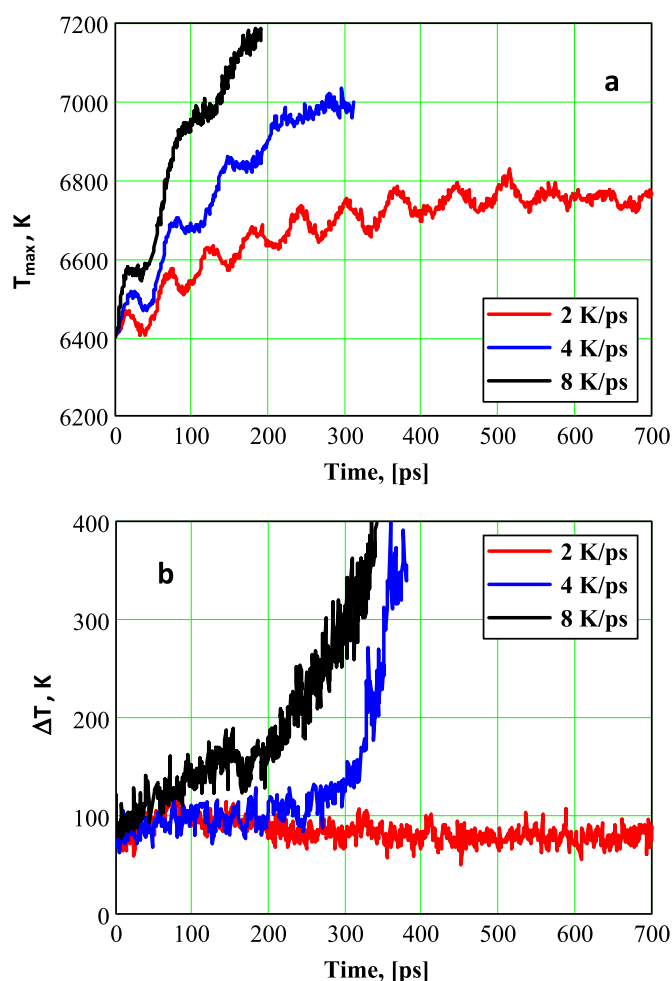


Figure 9. Maximal film temperature (a) and its fluctuations (b) at different heating rates.

4. Conclusion

The results presented in this paper and in [14] show that in the nanosecond ablation regime explosive boiling pressure pulses have a duration of about 0.3 ns and their amplitude considerably exceeds the surface evaporation pressure. No such pressure pulses have been observed up to now except for the case of subnanosecond pulses in water irradiated with erbium laser pulse [12]. It should be mentioned that in the case of the laser action on absorbing half-space, several repeated volume explosions can occur [2] if the laser pulse is not very short. Further experimental and theoretical investigations of explosive boiling during laser ablation process are needed to find the optimal regimes for obtaining new information about possible manifestation of the critical parameters in such experiments.

Acknowledgments

This work was partially supported by Russian Fund for Basic Research grants No. 13-02-01129, 13-07-00597, 15-07-05025.

References

- [1] Batanov V A, Bunkin F V, Prokhorov A M and Fedorov V B 1973 *Sov. Phys. JETP* **36** 311
- [2] Samokhin A A 1975 *Sov. J. Quantum Electron.* **4** 1144
- [3] Bulgakova N M and Bulgakov A V 2001 *Appl. Phys. A* **73** 199
- [4] Lu Q, Mao S, Mao X and Russo R 2002 *Appl. Phys. Lett.* **80** 3072
- [5] Andreev S N, Mazhukin V I, Nikiforova N M and Samokhin A A 2003 *Quantum Electron.* **33** 771
- [6] Garrison B J, Itina T E and Zhigilei L V 2003 *Phys. Rev. B* **68** 041501
- [7] Ivanov D S and Zhigilei L V 2003 *Phys. Rev. B* **68** 064114
- [8] Poneala C and Willis D A 2006 *Int. J. Heat Mass Transfer* **49** 1928

- [9] Poneala C and Willis D A 2009 *J. Phys. D: Appl. Phys.* **42** 155503
- [10] Zhakhovskii V V, Inogamov N A, Petrov Y V, Ashitkov S I and Nishihara K 2009 *Appl. Surf. Sci.* **255** 9592
- [11] Ionin A A, Kudryashov S I, Seleznev L V and Sinitsyn D V 2011 *JETP Lett.* **94** 753
- [12] Samokhin A A, Il'ichev N N, Klimentov S M and Pivovarov P A 2011 *Appl. Phys. B* **105** 551
- [13] Mazhukin V I, Samokhin A A, Demin M M and Shapranov A V 2014 *Mathematica Montisnigri* **29** 68
- [14] Mazhukin V I, Shapranov A V, Samokhin A A and Ivochkin A Y 2013 *Mathematica Montisnigri* **27** 65
- [15] Ionin A A, Kudryashov S I, Seleznev L V, Sinitsyn D V, Bunkin A F, Lednev V N and Pershin S M 2013 *JETP* **116** 347
- [16] Wu C and Zhigilei L V 2014 *Appl. Phys. A* **114** 11–32
- [17] Kartashov I N, Samokhin A A and Smurov I Y 2005 *J. Phys. D: Appl. Phys.* **38** 3703
- [18] Samokhin A A 1990 *Proc. of Inst. of Gen. Phys. (USSR: Academy of Sciences)* **13** pp 3
- [19] Mazhukin V I, Mazhukin A V and Lobok M G 2009 *Laser Physics* **19** 1169
- [20] Mazhukin V I, Nossov V V, Smurov I and Flamant G 2004 *J. Phys. D: Appl. Phys.* **37** 185
- [21] Mazhukin V I, Nossov V V and Smurov I 2007 *J. Appl. Phys.* **101** 024922